













Cite this: *Polym. Chem.*, 2025, **16**, 345

3D printable biopolymers as pelvic floor scaffolds†

Lindsay B. Chambers, ^{‡a} Yuxiang Zhu, ^{‡b} Churan Yu, ^a Natalie Crutchfield, ^e Jixin Hou,^a Liang Liang,^c Xianqiao Wang, ^d Yang Liu, ^e M. Taylor Sobczak, ^a Taylor Theobald,^a Xiao Sun,^f Carly R. Stoll,^g Tiffany V. Pulido,^g Johnny Yi,^h Jeffrey L. Cornella,ⁱ Heather McIlwee,^j Hitesh Handa, ^e Elizabeth J. Brisbois, ^e Jessica N. Lancaster^g and Kenan Song ^{*,l}

Pelvic floor disorders (PFD) are common among women, causing dysfunction, incontinence, and discomfort. Surgeries to repair the descended tissues can result in complications due to implant material design, particularly from the hardness and mechanical mismatch to native tissue. A more flexible implant could reduce complications, such as exposure and tissue erosion. This work seeks to characterize a 3D-printed double-crosslinked hydrogel tissue scaffold consisting primarily of polyvinyl alcohol (PVA). It also compares its static/dynamic/thermal/biological properties to existing commercial products used in PFD therapies, showing our pelvic mesh's biodegradability/robustness advantages over the commercial ones. Tensile tests revealed that the hydrogel scaffold was more compliant than the commercial alternatives. Dynamic mechanical testing has shown that these polymers are durable enough to support organs with specific weight above the pelvic floor. *In vivo* mouse studies demonstrated low inflammation and good biocompatibility over a 28-day period. The development of this scaffold offers a promising alternative for more effective, long-lasting PFD treatments with fewer post-operative complications, advancing personalized medicine.

Received 3rd October 2024,
Accepted 15th November 2024

DOI: 10.1039/d4py01103a

rsc.li/polymers

1 Introduction

Pelvic organ prolapse (POP) is a severe condition impacting millions of women globally, often resulting from childbirth, aging, or obesity.^{1,2} This disorder leads to the weakening of pelvic floor muscles, causing the pelvic organs to descend and bulge into or outside the vaginal canal, significantly affecting the quality of life.¹ The current state-of-the-art in treating POP involves a combination of advanced surgical techniques and innovative materials designed to reinforce or replace weakened pelvic floor tissues.³ Synthetic meshes such as polypropylene (PP), polyester (PET), and polytetrafluoroethylene (ePTFE) have been commonly used due to their strength, but high complication rates have led to declining use and FDA bans on PP for transvaginal repairs.⁴ Natural and biodegradable polymers such as collagen, alginate,⁵ and gelatin⁶ are emerging as promising alternatives due to their biocompatibility and ability to support cell attachment and tissue integration.⁷ However, these natural system-derived polymers usually do not have the mechanical durability to support organs above the pelvic floor.⁸ PVA, on the other hand, is compatible with different polymer chemistry and tunable for varying mechanical and functional properties, and thus has been chosen for this scaffold design because it has been a well-known biocompatible polymer for many years, and has been combined with chit-

^aDepartment of Mechanical Engineering, School of Environmental, Civil, Agricultural & Mechanical (ECAM), College of Engineering, University of Georgia, Athens, GA, 30602, USA

^bSchool of Manufacturing Systems and Networks, Ira A. Fulton Schools of Engineering, Arizona State University, Mesa, AZ, 85212, USA

^c123Techs Inc., Athens, GA, 30602, USA

^dSchool of Environmental, Civil, Agricultural & Mechanical (ECAM), College of Engineering, University of Georgia, Athens, GA, 30602, USA

^eDepartment of Biomedical Engineering, School of Chemical, Materials, and Biomedical Engineering (CMBE), College of Engineering, University of Georgia, Athens, GA, 30602, USA

^fDepartment of Mechanical and Industrial Engineering, College of Engineering, Northeastern University, Boston, MA, 02115, USA

^gDepartment of Immunology, Mayo Clinic Arizona, 13400 E Shea Blvd, Scottsdale, AZ, 85259, USA

^hDepartment of Obstetrics and Gynecology, Mayo Clinic Arizona, 13400 E Shea Blvd, Scottsdale, AZ, 85259, USA

ⁱDepartment of Medical and Surgical Gynecology, Mayo Clinic Arizona, 5777 E Mayo Blvd, Phoenix, AZ, 85054, USA

^jUniversity of Maryland Upper Chesapeake Medical Center, Bel Air, MD, 21014, USA

^kSchool of Environmental, Civil, Agricultural & Mechanical (ECAM), College of Engineering, University of Georgia, Athens, GA, 30602, USA.

E-mail: kenan.song@uga.edu

^lRegenerative Bioscience Center, UGA, Athens, GA, 30602, USA

†Electronic supplementary information (ESI) available. See DOI: <https://doi.org/10.1039/d4py01103a>

‡Co-first author.

osan,⁹ gelatin,¹⁰ and other natural molecules.¹¹ Moreover, PVA's versatility in biomedical applications,¹² especially in tissue engineering, has been demonstrated in various studies, highlighting its potential for creating scaffolds that offer both flexibility and durability. PVA-based hydrogels have been extensively used in soft tissue engineering, including cartilage repair,¹³ due to their ability to mimic the viscoelastic properties of native tissues.¹⁴ Furthermore, PVA is commonly utilized in drug delivery systems,¹⁵ where its biocompatibility and tunable degradation rates allow for controlled release of therapeutic agents over time. In clinical applications, PVA has been applied in vascular grafts,¹⁶ artificial corneas,¹⁷ liver tissue engineering,¹⁸ and wound dressings,¹⁹ with significant success in enhancing tissue regeneration and minimizing immune responses. Additionally, PVA-based materials have been explored in ophthalmology for use in contact lenses and eye implants due to their non-toxic, hydrophilic, and oxygen-permeable properties.²⁰

Advanced manufacturing techniques allow for the precise fabrication of custom-designed scaffolds that match patient anatomy, incorporating complex structures with controlled porosity and mechanical properties.²¹ For example, electrospinning and hybrid scaffolds that combine natural and synthetic materials are also being explored to enhance mechanical strength and biocompatibility.²² Additionally, bioactive scaffolds that include growth factors,²³ anti-inflammatory agents,²⁴ or antibiotics²⁵ are being developed to promote tissue healing and prevent complications. Regenerative medicine approaches, including stem cell therapy and tissue engineering,²⁶ are further advancing the field by enhancing the regenerative potential of scaffolds and promoting long-term functionality, aiming to improve patient outcomes and quality of life while minimizing risks associated with traditional synthetic meshes.

3D printing, also known as additive manufacturing, encompasses a variety of techniques such as stereolithography (SLA), fused deposition modeling (FDM), and direct ink writing (DIW), which build structures layer by layer from digital models. This technology enables the precise fabrication of complex and customized geometries, making it particularly advantageous for personalized medicine.²⁷ In the context of regenerative medicine, 3D printing can produce patient-specific implants, tissue scaffolds, and drug delivery systems tailored to individual anatomical and physiological needs. However, a significant challenge remains in the selection of materials that not only provide the necessary mechanical support but also degrade at appropriate rates within the body.²⁸ Many 3D printing materials still lack biodegradability, which is crucial for applications where the scaffold needs to be absorbed and replaced by natural tissue over time.²⁹ Ensuring that printed constructs can degrade safely without eliciting adverse reactions is essential for the successful integration and long-term efficacy of 3D-printed biomedical devices in regenerative therapies.

Understanding the mechanical and thermal properties of new biomaterials for the POP mesh prototype is critical for

benchmarking it against both experimental prototypes and commercially available meshes. Tensile strength, porosity, and swelling capabilities are important factors that contribute to the effectiveness of a tissue scaffold, particularly for applications such as pelvic floor repair and hernia treatment. These mechanical features influence the mesh's ability to support tissues while integrating seamlessly with the body's natural structures. For instance, porosity plays a significant role in enabling nutrient exchange and promoting cell proliferation, while tensile strength ensures the scaffold can withstand physiological stresses without causing damage to surrounding tissues.³⁰ Additionally, a material's swelling behavior affects its integration with soft tissues, contributing to the scaffold's biocompatibility and long-term functionality.²⁷ Given the limitations of current synthetic meshes, which often cause mechanical mismatches leading to complications, such as inflammation or erosion, there is a strong market demand for more flexible and biocompatible options that can effectively support pelvic organs.

This project seeks to address the challenges faced by current PFD treatments by introducing a novel, in-house synthesized PVA tissue scaffold with dual crosslinking strategies, designed to improve mechanical and biological performance. In this study, we have mechanically, thermally, and biologically characterized our PVA scaffolds, comparing them to some commercially available alternatives used for PFD repairs. Key techniques, such as tensile testing, dynamic mechanical analysis (DMA), and thermal stability tests, were used to assess the durability and compliance of the scaffolds. In addition, *in vivo* tests were conducted to evaluate cell viability, biodegradability, and inflammation response. By comprehensively characterizing these properties, this work aims to develop a superior tissue scaffold that can better mimic native tissues while offering customizable degradation profiles and enhanced biocompatibility. This approach is a promising step toward more personalized and effective treatments for pelvic floor disorders and other soft tissue injuries. More importantly, the combination of 3D printing and tissue engineering has the potential to revolutionize the field of regenerative medicine, offering a promising avenue for repairing or replacing damaged tissues that contain cellular structures more closely replicating the body's natural cellular architecture.

2 Experimental section

2.1 Materials

Raw materials including PVA. Kuraray America Inc. graciously supplied PVA (M_w 205k, partially hydrolyzed grades). We acquired various chemicals including *p*-toluenesulfonic acid (*p*TsOH, ACS reagent, 98.5%), anhydrous DMSO (99.9%), dithiothreitol (DTT, 97%), lithium phenyl-2,4,6-trimethylbenzoylphosphinate (LAP, 95%), *cis*-5-norbornene-*endo*-2,3-dicarboxylic anhydride (99%), citric acid (ACS reagent, 99.5%), sodium hydroxide pellets (reagent grade, 98%), microcrystalline cellulose (20 μ m), and sodium bicarbonate (NaHCO_3), all



of which were procured from Millipore Sigma. Additionally, SnakeSkin Dialysis Tubing (3.5K MWCO, 22 mm) was obtained from Thermo Fisher Scientific.

Functionalized PVA (fPVA). A mixture of 10 g PVA and 20 mg *p*TsOH was dissolved in 200 mL DMSO at 50 °C under a nitrogen atmosphere. Separately, 2 g *cis*-5-norbornene-*endo*-2,3-dicarboxylic anhydride was dissolved in 20 mL DMSO. This solution was gradually added to the PVA/*p*TsOH mixture. The reaction was maintained at 50 °C for 12 hours. The resulting crude product was placed in a dialysis tubing with a 3.5 kDa cutoff. Dialysis was performed against 100 mM NaHCO₃ for 12 hours and then against deionized water for 24 hours. Finally, the products were lyophilized to obtain fPVA.

3D printing inks. To prepare the fPVA solution, it was dissolved in deionized water at 60 °C with continuous magnetic stirring overnight, achieving a concentration of 12 wt%. Once fully dissolved, DTT and LAP were introduced to the mixture, maintaining a thiol-to-ene stoichiometric ratio of 4:10 and a photoinitiator (LAP) concentration of 0.05 wt%. The final feedstock, including 9 wt% cellulose powder as a rheology modifier, was termed fPVA/C. For the printing setup, a Hyrel 30 M system was adapted, using a pneumatic dispenser (Ultimus I, Nordson EFD) to extrude the ink through 30G nozzles at a pressure of 75 psi. Nozzle speeds were set to 45, 60, and 90 mm min⁻¹, with layer thicknesses of 0.08, 0.1, and 0.14 mm, respectively. A 50 W UV light (365 nm, Everbeam) was positioned above the printing bed to cure the ink *in situ* during the printing process. To prevent premature curing, the syringe was wrapped in aluminum foil (Fig. 1).

2.2 NaOH-XL-fPVA

The double network PVA was produced by submerging the UV crosslinked fPVA in a 6 M NaOH solution, and then stabilizing it in deionized water. A strong base is necessary to deprotonate the alcohol groups on the PVA strands.³¹ Throughout the entire study, these 3D printable meshes will be referred to as PVA samples.

2.3 Past commercial POP meshes as control samples

We have obtained from clinicians various materials used in pelvic organ prolapse (POP) tissue scaffolds, comparing our in-house synthesized PVA (NaOH-XL-fPVA) with several commercial meshes such as Progrid, Ventralight, Biodesign, 3DMax, Restorelle, and Vertessa, as shown in Table 1.

2.4 Characterizations

Tensile testing was performed using a Discovery HR2 from TA Instruments. Before testing, the mesh samples were hydrated in deionized water for 2 hours or according to the manufacturer's guidelines to ensure consistent preparation across materials. Tensile tests performed on the commercially available mesh were done with a Discovery DHR-2 strain rate of 100 mm s⁻¹ with an initial gap of 1 cm, and the final gap length was set to 5 cm to ensure complete bifurcation.

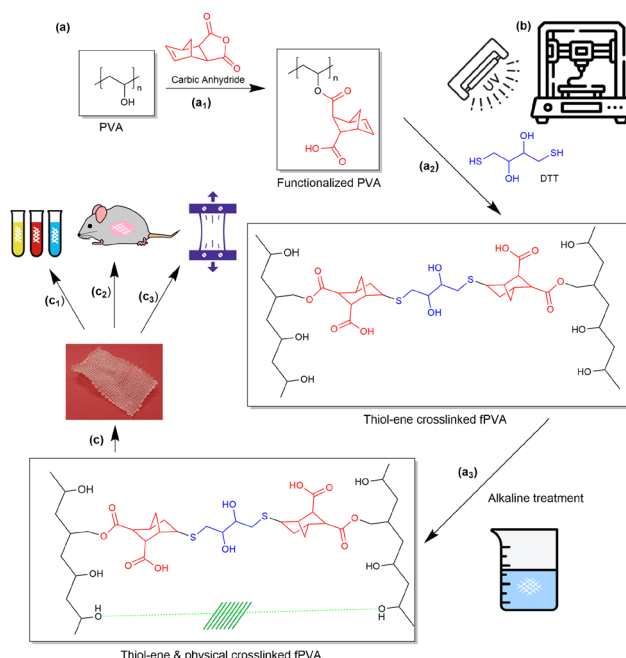


Fig. 1 Schematic representation of programmable PVA cross-linking and 3D printing of tissue scaffolds. (a) Polymer chemistry: (a1) functionalization of PVA with carboxylic anhydride to yield fPVA, (a2) initial cross-linking via DTT reaction, and (a3) subsequent thiol-ene cross-linking and physical cross-linking. (b) 3D printing process facilitated by UV light for precise dimensional control. (c) Characterization of fabricated tissue scaffolds, including mechanical properties, thermal stability, and cell viability/*in vivo* testing.

Samples were secured with tape and cardboard to minimize damage or slippage caused by the tension geometry apparatus. To calculate the amount of stress applied to the actual material, the cross-sectional area was corrected in the final measurements by dividing the calculated stress value by the area of the sample. The cross-sectional area was calculated by using ImageJ with Leica light microscope images (Fig. 2). The tensile modulus was collected from the linear elastic region from the stress/strain curve for each sample. **DMA** was performed *via* Discovery HR-2 from TA Instruments. The testing protocol began at room temperature with a temperature increase of 3 °C per minute, continuing until a final temperature of 140 °C was reached. The tests were performed with an axial displacement of 50 microns and a frequency of 1.0 Hz. All specimens were soaked appropriately before testing. **Thermogravimetric analysis (TGA)** was performed from room temperature to 900 °C, with a heating rate of 10 °C per minute. The weight loss of the samples was recorded as a function of temperature to assess thermal stability. **Differential scanning calorimetry (DSC)** analysis was carried out using a Discovery DSC 250 from TA Instruments, with a temperature ramp of 10 °C min⁻¹ from room temperature to the samples' respective degradation temperatures. The samples were then cooled at the same rate to 25 °C and then heated again to the degradation rate.



Table 1 A summary of PVA mesh properties as a comparison to commercial POP meshes, including previously FDA-approved and banned products. PP, polypropylene; PGA, polyglycolic acid; HA, sodium hyaluronate; CMC, carboxymethylcellulose; PEG, polyethylene glycol; PLA, polylactic acid; PVA, polyvinyl alcohol. Glass transition temperature (T_g) is the temperature detected by DSC at which a material has a more flexible consistency. A glass transition point was not observed in every sample, which could have occurred outside the range of analysis. Melting point (T_m) is when a material moves from solid to liquid state, detected by DSC. Because of the bonds between some polymers in a crosslinked material, melting points are not in all samples. Degradation temperature (T_d) is the point where degradation occurs in an inert environment, detected from the weight loss derivative to temperature in TGA. Elastic modulus is the slope of the stress/strain curve in the elastic region of the ultimate tensile tests. Tensile strength refers to maximum stress a sample can experience before breaking. Toughness was calculated by the area under the stress/strain curve and reported as kJ m^{-3} . These values were measured from simple tension tests. Storage modulus (E') and loss modulus (E''), were collected from the DMA curves at room temperature, and reflect the energy absorption or dissipation capabilities of the POP meshes. The last column includes the temperature and $\tan(\delta)$ values at their peak maxima

Samples	Materials	Thermal properties			Mechanical properties			Dynamic properties		$\tan \delta$	
		T_g ($^{\circ}\text{C}$)	T_m ($^{\circ}\text{C}$)	T_d ($^{\circ}\text{C}$)	Elastic modulus (MPa)	Strength (MPa)	Toughness (MJ m^{-3})	E' (MPa) at RT	E'' (MPa) at RT	Peak value	$^{\circ}\text{C}$
Vertessa	PP/non-absorbable	−10 (ref. 49)	172	310	94.65 ± 6.88	27.12 ± 1.24	0.31 ± 0.03	35.06	7.85	0.23	53
Restorelle	PP/non-absorbable	−10 (ref. 49)	169	367	76.37 ± 14.81	24.47 ± 3.69	0.29 ± 0.11	28.71	5.29	0.18	38
3DMax	PP/non-absorbable	−10 (ref. 49)	167	277	29.17 ± 2.77	21.61 ± 3.00	0.38 ± 0.07	11.03	4.23	0.39	N/A
Ventralight	PP and PGA knitted together. PGA surface coating is HA, CMC, and PEG based hydrogel/mesh is non-absorbable, hydrogel barrier resorbs within 30 days	PP −10 (ref. 49) PGA 35–40(ref. 50)	56, 169	178, 360	6.52 ± 0.87	4.99 ± 0.45	0.14 ± 0.02	41.44	10.71	0.25	58
Progrip	Monofilament PP for textiles and PLA as microgrips with fast resorbing film of 70% collagen and 30% glycerol/partially absorbable	75	168	294, 396	39.46 ± 4.56	9.02 ± 1.59	0.06 ± 0.02	280.63	28.57	0.10	N/A
Biodesign	Porcine small intestine submucosa/fully biodegradable	N/A	N/A	75, 242	62.26 ± 7.18	27.48 ± 1.39	0.24 ± 0.03	109.17	25.00	0.22	N/A
PVA	NaOH-fPVA/no cytotoxic effects observed after 28 days of implantation	45	N/A	81, 225, 463	4.88 ± 1.88	2.12 ± 0.29	0.02 ± 0.01	38.07	7.64	0.33	45

3 Results and discussion

3.1 An overview of 3D printable PVA tissue scaffolds

Previous commercial POP tissue scaffolds, particularly those composed of PP, have demonstrated issues with excessive rigidity,^{32,33} leading to mechanical incompatibility with the softer, native tissues they are designed to support.³⁴ This mechanical mismatch frequently results in acute or chronic inflammation and tissue erosion, significantly complicating patient recovery.³⁵ To overcome these limitations, new compliance-tunable biopolymers³⁶ are being developed, offering improved flexibility, reduced inflammation, and the potential to adjust mechanical properties to better align with the natural tissue environment.³⁷ These advanced materials provide a more biocompatible alternative for POP treatment, addressing both structural and biological needs.

This project centers on creating advanced tissue scaffolds for POP treatment using PVA as the primary polymer, enhanced through innovative crosslinking strategies. The PVA scaffold not only has enough supportive properties without much rigidity, but also strikes a balance between mechanical properties, especially structural support, and excellent biocompatibility.

To further diversify the functionality of PVA in the development of tissue scaffolds, various crosslinking strategies can be

employed. Chemical crosslinking using agents such as hydroxyapatite³⁸ or boric acid³⁹ is commonly used to improve the mechanical strength and stability of PVA hydrogels. Physical crosslinking methods, such as freeze–thaw cycles,⁴⁰ allow for the formation of crystalline regions within the PVA matrix, enhancing its tensile strength and elasticity without the need for additional chemical agents. In this study, the process involves a stepwise modification of PVA to increase its crosslinking capabilities. Initially, carboxylic anhydride (Fig. 1a1) functionalizes the PVA, providing reactive sites for subsequent crosslinking steps. Our choice of carboxylic anhydride over other chemicals was carefully made: in addition to the universal advantages of all thiol–ene reactions, such as robustness and insensitivity to oxygen inhibition,⁴¹ norbornene groups exhibit faster reaction rates with thiols compared to other vinyls (e.g. allylic derivatives and vinyl ethers).⁴² Moreover, the polymerization rate scales approximately with the 1/2 order in both thiol and ene functional group concentrations,⁴³ favoring stoichiometric polymerization,⁴³ favoring stoichiometric polymerization.⁴⁴ These advantages, along with the general benefits of thiol–ene reactions, make the thiol–norbornene system widely used in tissue engineering and regenerative medicine.⁴⁵ It has also been reported to work with other biomaterials, such as polyethylene glycol,⁴⁶ hyaluronic acid,⁴⁷ and gelatin.⁴⁸ The introduction of DTT initiates thiol–



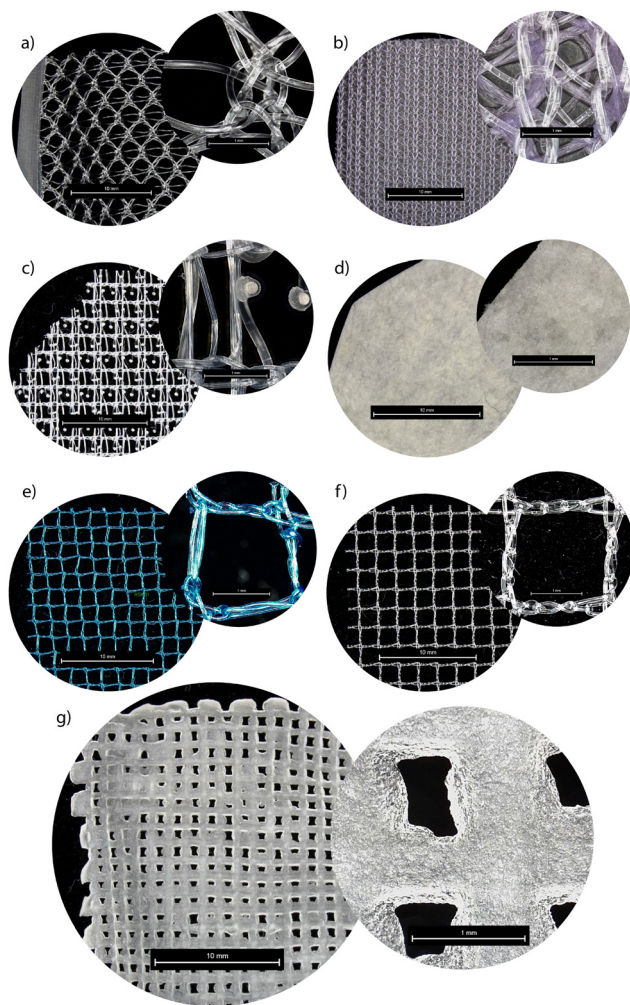


Fig. 2 (a) 3DMax, (b) Ventralight, (c) Progrid, (d) Biodesign, (e) Vertessa, (f) Restorelle, and (g) PVA scaffold. Scale bars on the left image pair represent 10 mm, and scale bars on the right image represent 1 mm. The average of 4 images for each sample was used to estimate porosity in the 2D cross-sectional area with ImageJ.

ene reactions (Fig. 1a2), forming a crosslinked network. This is further strengthened by a second physical crosslinking phase involving alkaline treatment (Fig. 1a3), resulting in a dual crosslinking structure that balances mechanical durability with controlled biodegradability. The physical crosslinking mechanism in our system arises from the crystallization of the PVA chains upon exposure to the alkaline environment, which was also confirmed with FTIR characterizations (Fig. S1†). When the PVA scaffold undergoes treatment with a strong base, the hydroxyl groups in PVA are deprotonated, which promotes the complexation³¹ between adjacent PVA chains. These hydrogen bonds result in the formation of crystalline regions within the polymer, known as physical crosslinking, because after the Na^+ ions are washed away, no new chemicals remain within the material. This process enhances the mechanical strength and structural integrity of the scaffold without the need for additional chemical crosslinkers. This dual cross-

linking strategy is key to producing a material that can endure the mechanical demands of pelvic organ repair while gradually degrading in a controlled manner as natural tissue regenerates.

3D printing plays a crucial role in the fabrication of these PVA-based scaffolds, allowing for precision control over scaffold microstructure, mechanical properties, and dimensional stability. The bioink feedstock is freshly prepared and loaded into a Hyrel printing system, where printing quality is continuously monitored through a camera to optimize the process at different pressures and speeds (Fig. 1b). UV light is employed to cure the scaffold during printing, initiating the first crosslinking phase, which imparts structural integrity to the construct. After printing three layers in the x - y direction, the scaffold undergoes the second crosslinking step in a NaOH bath, further reinforcing the mechanical properties. This dual crosslinking approach enhances scaffold strength while allowing for tunable degradation, ensuring that the scaffold can support tissue regeneration over time. Ongoing research focuses on the scaffolds' ability to promote tissue regeneration and their degradation profiles within the body, with early results showing significant promise in providing a more adaptive and biocompatible solution for POP repair (Fig. 1c). Due to the complex porous structures present in POP mesh, surface morphology was also examined using an optical microscope to obtain a more accurate estimation of the density and structural modifications of the tested samples (Fig. 2). Fig. 2 highlights the structural differences between various commercially available meshes used for POP repair, including our in-house synthesized PVA mesh (Fig. 2g). Unlike the knitted or woven patterns observed in commercial meshes such as Ventralight (Fig. 2b), Progrid (Fig. 2c), and Restorelle (Fig. 2f), the PVA scaffold exhibits a highly regular grid structure. This regularity simplifies the evaluation of mechanical and other material properties, as it eliminates the complexities arising from non-uniform weaving patterns found in traditional meshes. The PVA mesh's uniform pore distribution ensures predictable deformation and mechanical behavior, which is crucial for ensuring the consistent performance required for pelvic floor repair. Additionally, precise control over porosity facilitates better nutrient flow and cell attachment, potentially leading to improved tissue integration. This approach allowed for a better understanding of surface features and potential variations in density that can influence the mechanical properties and overall performance of the mesh.

3.2 Thermal stability and biodegradability

Our in-house synthesized PVA mesh demonstrates excellent biocompatibility, as demonstrated in our previous cellular studies.⁵¹ This contrasts with several other polymers previously used in clinical curing (Table 1), such as the non-absorbable PP-based commercial meshes Vertessa, Restorelle, and 3DMax, which are durable but present challenges namely chronic inflammation due to their mechanical mismatch with native tissues. Ventralight and Progrid utilize combinations of absorbable and non-absorbable components, including PP



and polyglycolic acid (PGA), allowing for partial absorption and resorption of barrier layers, offering a balance between structural support and reduced long-term foreign body response. However, these POP meshes are not fully biodegradable, which often necessitates a second surgery for removal, potentially leading to additional complications and side effects. On the other hand, Biodesign, composed of porcine small intestine submucosa, is fully biodegradable, providing complete integration with host tissues but may lack long-term mechanical durability. These comparisons in Table 1 emphasize the potential of our PVA-based scaffolds to offer both biocompatibility and tunable thermal stability and degradation, essential for personalized treatments in POP. The general thermal property values in Table 1 are from DSC/TGA tests, as plotted in Fig. 3.

TGA results. TGA is essential for assessing the thermal stability and degradation profile of polymers before conducting DSC, ensuring that the appropriate temperature ranges are identified. In the case of the PVA tissue scaffold, TGA revealed multiple degradation events (Fig. 3a). The initial degradation, observed at 81 °C, corresponds to the evaporation of water absorbed from environmental humidity. The second significant degradation event, occurring at 225 °C, is attributed to the thermal breakdown of PVA. This is followed by a third degradation event around 465 °C, which indicates the decomposition of microcrystalline cellulose (MC)⁵² present in the scaffold as a reinforcing filler. These results underscore the scaffold's composition and the roles that different constituents play in its thermal behavior. In comparison, Progrid, primarily composed of PP and polylactic acid (PLA), shows two distinct degradation peaks at 294 °C and 396 °C, highlighting the thermal decomposition of each polymer component. Ventralight, consisting of PP and PGA, exhibited degradation peaks at 178 °C and 360 °C, consistent with the known melting point of PGA at 225 °C.⁵³ Other commercial meshes such as 3DMax, Vertessa, and Restorelle, which are primarily composed of PP, demonstrated single degradation peaks at 277 °C, 310 °C and 367 °C respectively, emphasizing the thermal stability of pure PP. These comparisons show that the degradation temperatures vary significantly based on the composition, offering insight into the scaffold's potential behavior during in-body use.

DSC results. The DSC analysis conducted on the PVA tissue scaffolds and various commercial meshes (such as Progrid, Ventralight, Biodesign, 3DMax, Restorelle, and Vertessa) reveals key differences in their thermal behaviors (Fig. 3b and c). Each sample was heated before its degradation temperature, cooled to room temperature, and then reheated to remove any residual water content. The in-house synthesized crosslinked PVA mesh exhibited no endothermic or exothermic peaks, indicating that the crosslinking process was thorough and complete, contributing to its stability under thermal conditions. In contrast, some commercial products such as Progrid and Ventralight, which contain additional materials such as PLA and PGA, exhibited specific thermal transitions related to their polymer components. For example, Progrid

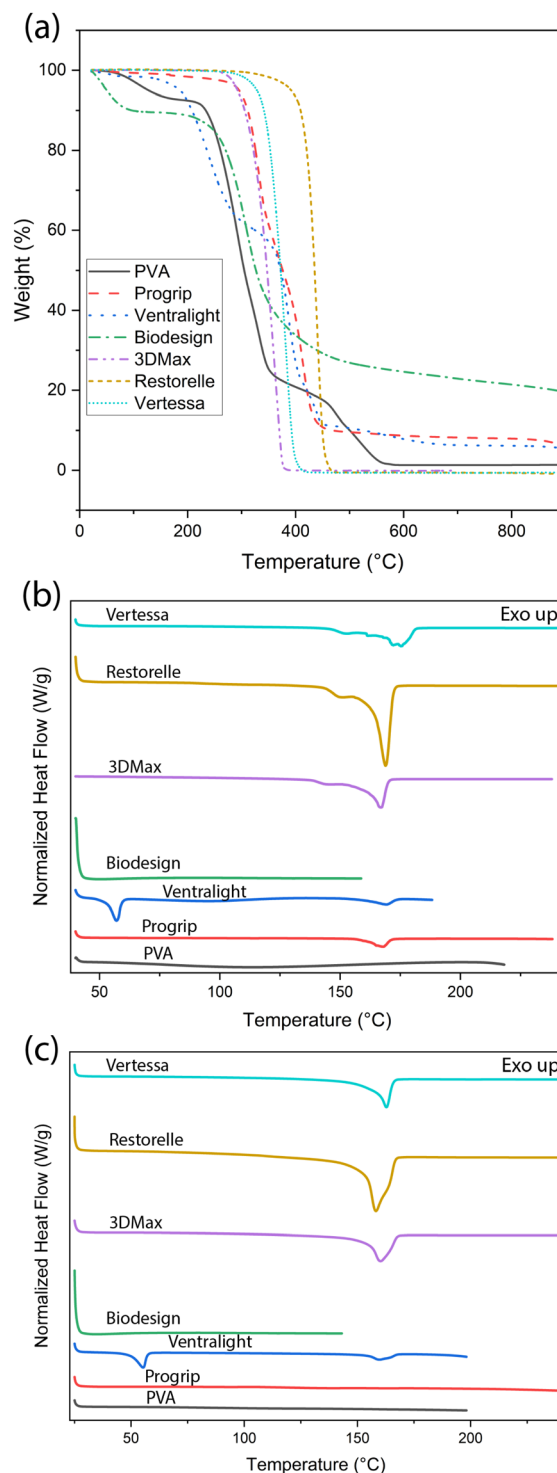


Fig. 3 (a) Thermogravimetric analysis (TGA) highlights the degradation points of various samples, including our in-house synthesized PVA, compared with commercial meshes such as Progrid, Ventralight, Biodesign, 3DMax, Restorelle, and Vertessa. (b) Differential scanning calorimetry (DSC) data, showing different transition points via the heating curves at a rate of 10 °C min⁻¹ until just before the degradation point of each sample. (c) After cooling to 25 °C, the samples were reheated under the same conditions to analyze thermal transitions and stability. Note: the DSC analysis for Biodesign, Ventralight, and PVA was shorter than for the other samples because they degraded at a lower temperature.



showed thermal behavior consistent with its partially absorbable nature, while Ventralight demonstrated characteristic transitions of its PP/PGA content (Table 1). The absence of melting peaks within short heating stages in the PVA mesh points to its unique advantage in maintaining consistent mechanical properties without significant thermal transitions, making it potentially more reliable for short-term organ support above the pelvic floor compared to traditional commercial meshes. However, the long-term PVA use in POP treatments will need to examine the degradation under proper conditions.

Biodegradability results. To ensure the PVA mesh is customizable for POP treatment, it is crucial to study the degradation behavior of the material under different environmental conditions (e.g., exposure to different in-body fluids and in different patients). The degradability tests were conducted by immersing PVA samples in deionized (DI) water and acetic acid solutions adjusted to a pH range of 4 to 7 (Fig. 4). The weight of each sample was recorded at the start of the experiment and then periodically throughout the study to monitor weight loss over time. The samples were weighed five times for each measurement to minimize variability. The data collected over several weeks, as shown in Fig. 4a, indicate that the degradation rate of PVA is highly dependent on pH levels. This is critical for POP tissue scaffolds, as biodegradability ensures that the scaffold supports tissue regeneration while gradually breaking down as the native tissue heals. The data demonstrates that at lower pH values, such as pH 4, the PVA degradation occurs more rapidly, with a significant weight loss observed within the first 20 days, indicating that more acidic environments accelerate the scaffold's breakdown. At higher pH values (pH 6 and 7), the PVA mesh maintains greater structural integrity, degrading more slowly and steadily over 30 days. This ability to control the degradation rate based on environmental conditions makes the PVA scaffold particularly versatile for personalized medicine, where the degradation profile can be tuned according to the specific needs of the patient and the targeted tissue environment.

Controlling the swelling ratio is crucial for POP tissue scaffolds as it directly affects the scaffold's ability to support tissue integration, nutrient transfer, and overall mechanical stability. The swelling ratio analysis (Fig. 4b) shows the ability

of various materials to absorb and retain fluids, which is critical for their performance as tissue scaffolds in POP treatments. Ventralight has the highest swelling ratio, indicating its significant ability to absorb fluids, which may facilitate nutrient transport and cell migration, making it suitable for tissue integration. In contrast, Ventralight, 3DMax, and Restorelle exhibit a very low swelling ratio, reflecting their non-absorbable nature, and thus limited interaction with surrounding tissues. Our in-house PVA mesh demonstrates a moderate swelling ratio of 2.31, indicating a balanced property that allows for tissue interaction without excessive swelling, which could cause mechanical instability. This is similar to Biodesign, made from porcine submucosa and showing a higher swelling ratio, favoring tissue compatibility. This comparison highlights the PVA scaffold's ability to offer a balanced approach between thermal stability/biological durability and adequate swelling properties, making it a promising candidate for POP repair.

3.3 Static mechanical tests

For all samples tested in this study, a representative stress/strain plot is shown in Fig. 5a, where the stepwise collapse of Ventralight is observed due to the nature of two different polymers being knitted together. Also, the tensile test curves for certain mesh samples, such as Restorelle and Vertessa, exhibit step-wise fractures with multiple peaks due to the individual breakage of filaments that constitute the mesh. These materials, as seen in the structural images above (Fig. 2), consist of woven or knitted networks of filaments. When subjected to tension, these networks do not fail uniformly. Instead, individual fibers within the mesh break progressively as the load increases, resulting in a step-wise fracture pattern. Each peak in the stress-strain curve corresponds to the sequential rupture of a group of filaments or individual threads in the mesh, leading to temporary stress relief before the next set of filaments begins to bear the load, creating another peak. This progressive failure mechanism is typical for woven or knitted structures, where different parts of the mesh engage or fail at different points in the deformation process. In contrast, the smooth and continuous curve seen in the PVA scaffold indicates a more homogeneous material response, likely due to its regular grid structure. The absence of distinct steps suggests that the PVA scaffold experiences more uniform stress distribution, without localized breakages common in more complex woven or knitted meshes. This feature of the PVA scaffold could be advantageous for predictable mechanical performance in medical applications.

The mechanical properties of the PVA-based scaffold show promising potential when compared to commercial mesh alternatives for POP treatment, particularly in terms of compliance and elastic modulus (Fig. 5b1 and 2). Commercial meshes such as Restorelle, 3DMax, Biodesign, and others exhibit higher elastic modulus values, with stiffer materials such as Vertessa having an elastic modulus of around 94.65 MPa and tensile strength of 27.12 MPa. These stiff materials, especially those made from PP, can lead to complications such

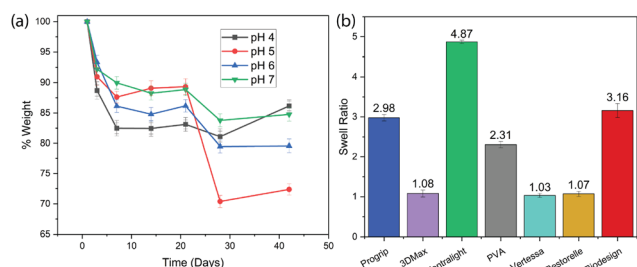


Fig. 4 (a) PVA mesh biodegradability in solutions of different pH values over time. (b) Swelling behaviors of all samples including our PVA and the commercial products.



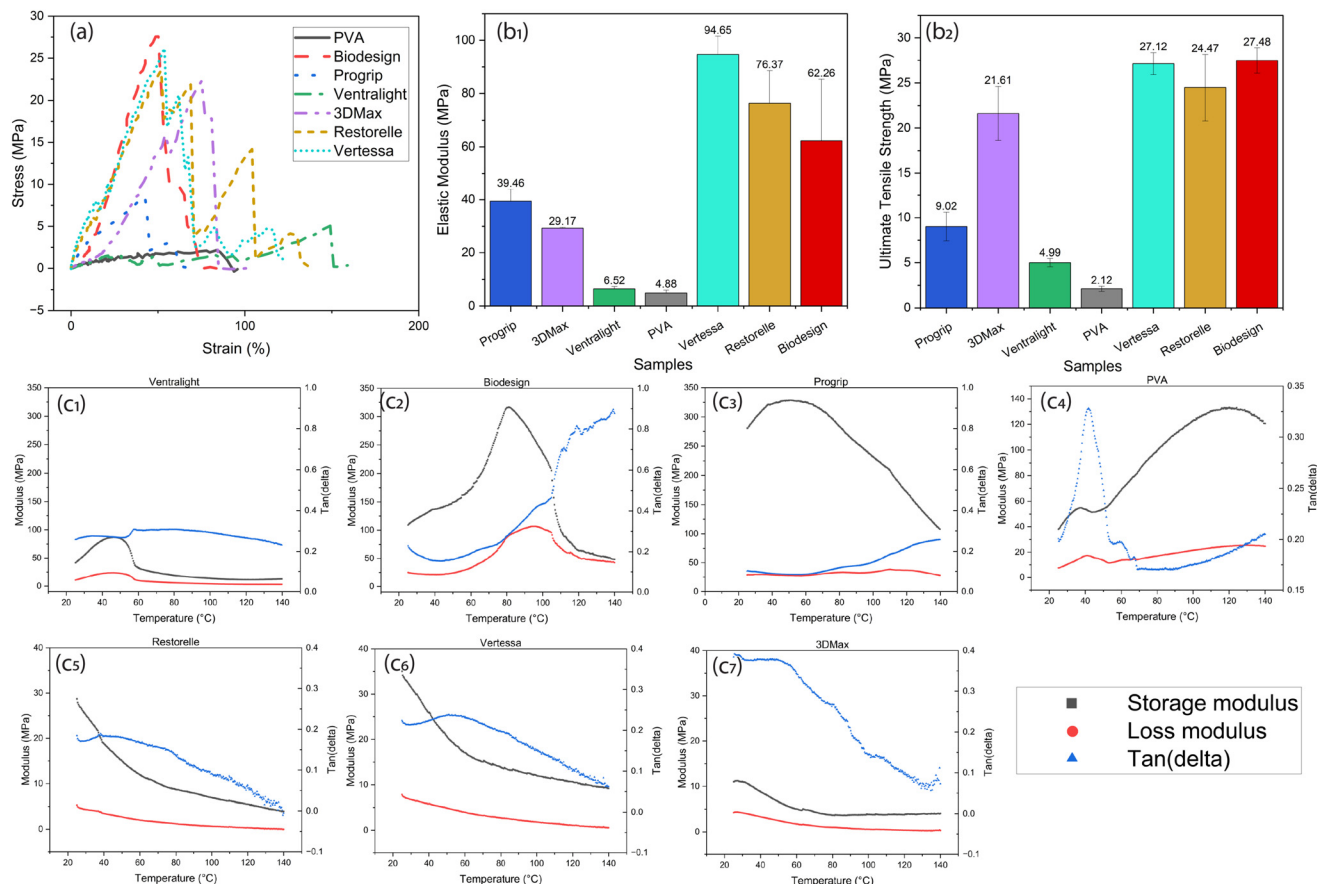


Fig. 5 (a) Example stress/strain plots for ultimate tensile strength testing. (b1) Average elastic modulus (b2) average elastic modulus calculated from the slope of the stress/strain plots. (c1–7) DMA plots.

as erosion and exposure due to their rigidity and mechanical mismatch with native tissues. In contrast, the PVA mesh developed in this study has a significantly lower elastic modulus of 4.88 MPa that can be tuned with different cross-linking densities, which is the same order of magnitude as the human pelvic floor modulus (*i.e.*, 1–15 MPa (ref. 54)), making it a better candidate for reducing inflammation and injury upon implantation. The lower modulus and higher compliance of the PVA mesh reduce the risk of sharp edges causing tissue damage, thus mitigating post-operative complications commonly seen with stiffer commercial meshes. Moreover, the softer nature of the PVA scaffold can adapt more readily to the dynamic environment of the pelvic floor, reducing the risk of erosion where the mesh might otherwise damage surrounding tissue. This compliance, combined with the scaffold's tuneable degradation properties, supports its potential for POP treatment, as it could provide temporary structural support while allowing for tissue regeneration and minimizing long-term complications. These properties suggest that the PVA scaffold offers a balance between mechanical strength and flexibility, making it a safer and more effective alternative for patients undergoing pelvic organ prolapse repair.

3.4 DMA

The DMA results provide key insights into the mechanical properties of the commercial meshes and the PVA tissue scaffold as a function of temperature (Fig. 5c). The storage modulus (E') for most samples remains relatively stable, reflecting their elastic behavior over a broad temperature range. However, in the case of the in-house synthesized PVA mesh (Fig. 5c4), there is a notable rise in the storage modulus at elevated temperatures, indicating that the material stiffens as it transitions into a more rigid state, likely due to water loss or changes in its polymer structure. This stiffening behavior is probably absent for pelvic floor applications, where the scaffold is immersed in a water environment and offers firm support while maintaining biocompatibility.

The loss modulus (E'') highlights the viscoelastic properties of the materials. The PVA mesh and Biodesign show pronounced peaks, indicating greater energy dissipation at higher temperatures. For the PVA sample, the increase in loss modulus corresponds to its transition from a softer, flexible state to a more rigid configuration as the material dries. The tan delta (δ), which is the ratio of the loss modulus to the storage modulus, provides further insight into the damping



characteristics of these materials. The PVA mesh shows a prominent peak in tan delta around 45 °C, suggesting that this could be a glass transition temperature (T_g) or a thermochemical change related to a degradation event, which aligns with thermal transitions observed in other studies.⁵⁵ This increase in tan delta represents a shift in material flexibility, reinforcing that PVA stiffens at higher temperatures. As compared, the DMA analysis of the polypropylene (PP)-based meshes' Restorelle, Vertessa, and 3DMax' shows consistent thermal and mechanical properties across all samples. The storage modulus steadily decreases with increasing temperature, reflecting the softening of the materials as they approach higher temperatures, while the loss modulus remains relatively low, indicating minimal energy dissipation. The tan(delta) curves exhibit small peaks around 50–60 °C, hinting at a minor thermal transition.

However, comparing the elastic modulus from tensile tests and the storage modulus from DMA can be challenging due to differences in sample preparation and the nature of the tests. For instance, during tensile testing, inconsistencies in the cross-sectional area due to variations in the knitting patterns of the commercial meshes lead to variability in the mechanical properties observed. Additionally, weaker fibers in the mesh may snap during testing, further altering the cross-sectional area and skewing the results. As a result, the elastic modulus from tensile tests may not always directly correlate with the storage modulus obtained through DMA. Also, the DMA results indicate that the in-house synthesized PVA mesh demonstrates enhanced storage modulus while maintaining stable loss modulus, particularly under elevated temperatures. This material's ability to balance stiffness and flexibility positions it as a promising alternative to commercially available meshes, which may suffer from mechanical mismatch with native tissues, leading to complications like inflammation.

Fatigue tests have also been conducted to evaluate the long-term performance and durability of materials under repeated mechanical stress, simulating the cyclic loads experienced by POP scaffolds in the body. These tests ensure that the scaffold can maintain structural integrity and functional support over prolonged periods of use. Fig. S3† showed that the PVA showed more consistent responses as compared to the commercial meshes, without little fluctuations or degradation during the fatigue cycles. As a result, the PVA scaffold demonstrates superior flexibility, durability, and fatigue resistance compared to commercial POP tissue scaffolds, with tensile, DMA, and fatigue test results showing enhanced mechanical compatibility with native tissue and reduced risk of complications. These results are also consistent with the literature reports (Table S1†).

3.5 In vivo tests in animal models

Assessment of intraperitoneal implantation into immunocompetent C57BL/6J mice demonstrated the biocompatibility of the PVA tissue scaffolds (Fig. 6). Abdominal placement loaded the mouse's body weight onto the scaffold, serving as a proxy for organ support in POP patients. Scaffold-implanted mice were compared to a surgical control (sham) group, in which

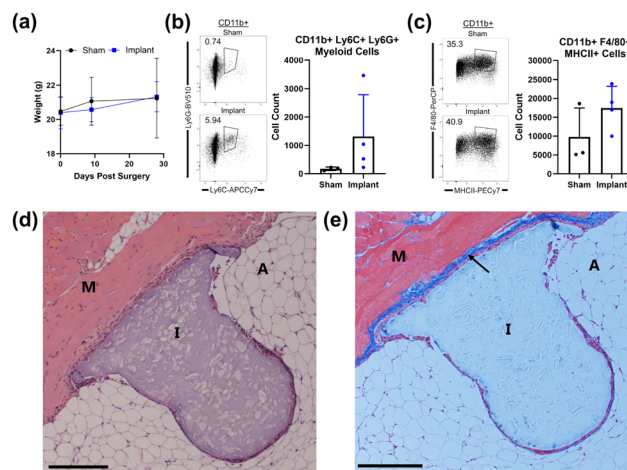


Fig. 6 (a) PVA scaffold implants were placed in four mice and monitored for 28 days. Implant and sham surgery groups were weighed at indicated time-points to monitor overall health. (b) At 28 days post-surgery, cells were collected *via* intraperitoneal (IP) lavage in both sham and implant experimental groups and analyzed by flow cytometry. Cells were sorted by size and live/dead markers, and then further by CD11b+ myeloid lineage. Cells were further sorted by Ly6C⁺ and Ly6G⁺ markers and the differences between sham and implant groups are shown. Cell count of CD11b+Ly6C⁺Ly6G⁺ myeloid cells was plotted showing a non-significant ($p = 0.2491$) increase in the implant group. (c) CD11b+ myeloid cells were sorted by F4/80 and MHC II, and sham vs. implant groups were compared. Cell count was plotted showing a non-significant increase of these cells ($p = 0.1877$). (d) Hematoxylin and eosin (H&E) stain of scaffold implant. Tolerance of the implant into the tissue is shown. M = muscle layer, A = adipose tissue, I = implant. Scale bar, 200 μ M. (e) Masson's trichrome (MT) stain of the same scaffold implant as (d). The arrow points to fibrosis and collagen formation as indicated by blue staining. Scale bar, 200 μ M. See Fig. S1† for more data and experimental details.

the intraperitoneal cavity was accessed but then sutured without implant placement. Post-operative monitoring revealed that scaffold-implanted mice exhibited minimal signs of distress as compared to sham controls, with no significant weight loss or abnormal behavior at 28 days post-surgery (Fig. 6a), indicating good tolerance to the implants. At the end-point of the experiment, cells were collected *via* intraperitoneal (IP) lavage and analyzed by flow cytometry. Flow cytometry data of IP fluid revealed only a slight, but not significant, increase in Ly6C⁺Ly6G⁺ myeloid cells ($p = 0.2491$) and F4/80⁺MHCII⁺ ($p = 0.1877$) macrophages as compared to sham controls, suggesting a mild and controlled inflammatory response (Fig. 6b and c). Scaffolds were recovered at the end-point and prepared for histological analysis. Hematoxylin and eosin (H&E) staining confirmed that muscle and adipose tissues surrounding the scaffolds maintained their integrity, with no distortions or accumulations of mononuclear cells detected around the scaffolds (Fig. 6d). Masson's trichrome (MT) staining confirmed minimal fibrosis surrounding the scaffold or in the surrounding tissue (Fig. 6e). Thus, histological analysis indicated that the PVA scaffolds were well-integrated with the surrounding tissues, with minimal fibrosis or inflammation observed. Overall, the PVA scaffolds supported



tissue maintenance without inducing significant adverse reactions, underscoring their potential as biocompatible materials for POP treatment. All animal procedures were performed in accordance with the Guidelines for Care and Use of Laboratory Animals of Mayo Clinic and approved by the Institutional Animal Care and Use Committee.

4 Conclusion

Our PVA scaffold exhibits a flexibility comparable to commercially available hernia mesh samples, but with designed, reduced stiffness and strength, which is critical for preventing tissue damage. The materials showed varying biodegradation rates, which is highly desirable for customized tissue scaffolds. The *in vivo* mice studies were promising, showing no signs of inflammation or tissue damage, and no infections were observed after the implantation. These results suggest that the material holds strong potential for safe use in medical applications. Future work will focus on varying the polymer chemistry and crosslinking strategies, as these biocompatible materials may further enhance tissue integration.

Author contributions

L. C. – data curation, formal analysis, investigation, methodology, resources, writing – review & editing. Y. Z. – conceptualization, data curation, investigation, methodology, resources, writing – original draft, review & editing. C. Y. – investigation, data curation, writing – review & editing. N. C. – data curation, investigation, methodology. J. H., L. L., X. W., Y. L., M. T. S., – writing – review & editing. T. T. – writing – review & editing, visualization. X. S., C. S., T. P., – data curation. J. Y., J. C., – conceptualization, resources, supervision. H. M. – resources. J. L. – conceptualization, methodology, resources, supervision, project administration. H. H., E. B., – supervision. K. S. – conceptualization, formal analysis, funding acquisition, investigation, methodology, project administration, resources, writing – original draft, review & editing.

Data availability

The data supporting this article have been included as part of the ESI.†

Conflicts of interest

There are no conflicts to declare.

Acknowledgements

Commercial samples Restorelle (Coloplast Corp. Minneapolis, MN), 3DMax (Bard Davol Inc. Warwick, RI), Ventralight (Bard

Davol Inc. Warwick, RI), and ProGrip (Medtronic Inc. Minneapolis, MN) were expired medical devices generously donated by the University of Maryland Upper Chesapeake Medical Center through surgical nurse Heather McIlwee. Dr Johnny Yi, MD generously donated remnant unusable commercial samples of Biodesign (Cook Biotech Inc. West Lafayette, IN) and Restorelle (to supplement the tensile test requirements) on behalf of the Operating Room supply at Mayo Clinic Arizona. Vertessa, a donation from Caldera Medical Inc. (Westlake Village, CA), was also collected by Dr Yi.

We appreciate the funding from the NSF CAREER (award # 2145895), AFOSR (award # FA9550-22-1-0263), Qatar National Research Fund (grant # NPRP14S-0317-210064), U.S. National Science Foundation EFRI (award # 2132183), AZBHS Early Investigator Award (N/A), Women and Philanthropy Foundation (WP) (N/A), and ASU-Mayo Collaboration Seed Grant (N/A).

References

- 1 M. Barber and C. Maher, *Int. Urogynecol. J.*, 2013, **24**, 1783–1790.
- 2 T. Henderson, K. L. Christman and M. Alperin, *Urogynecology*, 2024, **30**, 519–527.
- 3 A. Giannini, M. Caretto, E. Russo, P. Mannella and T. Simoncini, *Climacteric*, 2019, **22**, 60–64.
- 4 C. J. Heneghan, B. Goldacre, I. Onakpoya, J. K. Aronson, T. Jefferson, A. Pluddemann and K. R. Mahtani, *BMJ Open*, 2017, **7**, 7.
- 5 T. Ramdhan, S. H. Ching, S. Prakash and B. Bhandari, *Trends Food Sci. Technol.*, 2020, **106**, 150–159.
- 6 P. S. Gungor-Ozkerim, I. Inci, Y. S. Zhang, A. Khademhosseini and M. R. Dokmeci, *RSC Biomater. Sci.*, 2018, **6**, 915–946.
- 7 F. Zhang and M. W. King, *Adv. Healthcare Mater.*, 2020, **9**, 1901358.
- 8 B. Gurumurthy and A. V. Janorkar, *Curr. Opin. Biomed. Eng.*, 2021, **17**, 100253.
- 9 K. G. Nathan, K. Genasan and T. Kamarul, *Mar. Drugs*, 2023, **21**, 304.
- 10 M. Sun, Y. Wang, L. Yao, Y. Li, Y. Weng and D. Qiu, *Polymers*, 2022, **14**, 1400.
- 11 S. Barbon, M. Contran, E. Stocco, S. Todros, V. Macchi, R. D. Caro and A. Porzionato, *Processes*, 2021, **9**, 730.
- 12 E. A. Kamoun, S. A. Loutfy, Y. Hussein and E.-R. S. Kenawy, *Int. J. Biol. Macromol.*, 2021, **187**, 755–768.
- 13 H. Li, C. Wu, X. Yu and W. Zhang, *J. Mater. Res. Technol.*, 2023, **24**, 2279–2298.
- 14 M. Bercea, L. M. Gradinaru, I. Plugariu, M. Mandru and D. L. Tigau, *Polym. Int.*, 2020, **69**, 149–155.
- 15 G. Rivera-Hernández, M. Antunes-Ricardo, P. Martínez-Morales and M. L. Sánchez, *Int. J. Pharm.*, 2021, **600**, 120478.
- 16 E. Dattola, E. I. Parrotta, S. Scalise, G. Perozziello, T. Limongi, P. Candeloro, M. L. Coluccio, C. Maletta,



- L. Bruno, M. T. De Angelis, G. Santamaria, V. Mollace, E. Lamanna, E. Di Fabrizio and G. Cuda, *RSC Adv.*, 2019, **9**, 4246–4257.
- 17 J. Wang, C. Gao, Y. Zhang and Y. Wan, *Mater. Sci. Eng., C*, 2010, **30**, 214–218.
- 18 S. Supriya Bhatt, G. Thakur and M. Nune, *Mater. Today: Proc.*, 2023, S2214785323007952.
- 19 S. G. Jin, *Chem. – Asian J.*, 2022, **17**, e202200595.
- 20 H. Jiang, Y. Zuo, L. Zhang, J. Li, A. Zhang, Y. Li and X. Yang, *J Mater Sci: Mater. Med.*, 2014, **25**, 941–952.
- 21 V. M. Vaz and L. Kumar, *AAPS PharmSciTech*, 2021, **22**, 49.
- 22 Y. Afsharian and M. Rahimnejad, *Polym. Test.*, 2021, **93**, 106952.
- 23 J. Lai, J. Li and M. Wang, *MRS Commun.*, 2020, **10**, 579–586.
- 24 T. Später, A. O. Mariyanats, M. A. Syachina, A. V. Mironov, A. G. Savelyev, A. V. Sochilina, M. D. Menger, P. A. Vishnyakova, E. Y. Kananykhina, T. K. Fatkhudinov, G. T. Sukhikh, D. D. Spitkovsky, A. Katsen-Globa, M. W. Laschke and V. K. Popov, *ACS Biomater. Sci. Eng.*, 2020, **6**, 5744–5757.
- 25 L. Visscher, H. Dang, M. Knackstedt, D. Hutmacher and P. Tran, *Mater Sci. Eng., C*, 2018, **87**, 78–89.
- 26 D. Howard, L. D. Buttery, K. M. Shakesheff and S. J. Roberts, *J. Anat.*, 2008, **213**, 66–72.
- 27 A. Souness, F. Zamboni, G. M. Walker and M. N. Collins, *J. Biomed. Mater. Res., Part B*, 2017, **106**, 533–545.
- 28 A. K. M. B. Khoda, I. T. Ozbolat and B. Koc, *J. Biomech. Eng.*, 2010, **133**, 011001.
- 29 M. Sheridan, L. Shea, M. Peters and D. Mooney, *J. Controlled Release*, 1999, **64**, 91–102.
- 30 D. P. Byrne, D. Lacroix, J. A. Planell, D. J. Kelly and P. J. Prendergast, *Biomaterials*, 2007, **28**, 5544–5554.
- 31 M. A. Darabi, A. Khosrozadeh, Y. Wang, N. Ashammakhi, H. Alem, A. Erdem, Q. Chang, K. Xu, Y. Liu, G. Luo, A. Khademhosseini and M. Xing, *Adv. Sci.*, 2020, **7**, 1902740.
- 32 A. Feola, S. Abramowitch, Z. Jallah, S. Stein, W. Barone, S. Palcsey and P. Moalli, *BJOG*, 2013, **120**, 224–232.
- 33 E. Mancuso, C. Downey, E. Doxford-Hook, M. G. Bryant and P. Culmer, *J. Biomed. Mater. Res.*, 2020, **108**, 771–789.
- 34 S. L. Edwards, J. A. Werkmeister, A. Rosamilia, J. A. Ramshaw, J. F. White and C. E. Gargett, *J. Mech. Behav. Biomed. Mater.*, 2013, **23**, 53–61.
- 35 A. Seifalian, Z. Basma, A. Digesu and V. Khullar, *Biomedicines*, 2023, **11**, 741.
- 36 S. R. Caliari and J. A. Burdick, *Nat. Methods*, 2016, **13**, 405–414.
- 37 J. L. Drury and D. J. Mooney, *Biomaterials*, 2003, **24**, 4337–4351.
- 38 D. Zhang, K. Chen, L. Wu, D. Wang and S. Ge, *J. Bionic Eng.*, 2012, **9**, 234–242.
- 39 A. Gupta, R. Kumar, N. K. Upadhyay, P. Surekha and P. K. Roy, *J. Appl. Polym. Sci.*, 2009, **111**, 1400–1408.
- 40 S. A. Bernal-Chávez, A. Romero-Montero, H. Hernández-Parra, S. I. Peña-Corona, M. L. Del Prado-Audelo, S. Alcalá-Alcalá, H. Cortés, L. Kiyekbayeva, J. Sharifi-Rad and G. Leyva-Gómez, *J. Biol. Eng.*, 2023, **17**, 35.
- 41 C. Hoyle and C. Bowman, *Angew. Chem., Int. Ed.*, 2010, **49**, 1540–1573.
- 42 *Radiation Curing of Polymeric Materials*, ed. C. E. Hoyle and J. F. Kinstle, American Chemical Society, Washington, DC, 1990, vol. 417.
- 43 N. B. Cramer, S. K. Reddy, A. K. O'Brien and C. N. Bowman, *Macromolecules*, 2003, **36**, 7964–7969.
- 44 J. A. Carioscia, L. Schneidewind, C. O'Brien, R. Ely, C. Feeser, N. Cramer and C. N. Bowman, *J. Polym. Sci., Part A: Polym. Chem.*, 2007, **45**, 5686–5696.
- 45 C. Lin, C. S. Ki and H. Shih, *J Appl. Polym. Sci.*, 2015, **132**, 41563.
- 46 B. D. Fairbanks, M. P. Schwartz, A. E. Halevi, C. R. Nuttelman, C. N. Bowman and K. S. Anseth, *Adv. Mater.*, 2009, **21**, 5005–5010.
- 47 W. M. Gramlich, I. L. Kim and J. A. Burdick, *Biomaterials*, 2013, **34**, 9803–9811.
- 48 Z. Muñoz, H. Shih and C.-C. Lin, *Biomater. Sci.*, 2014, **2**, 1063–1072.
- 49 E. Passaglia and H. K. Kevorkian, *J. Appl. Phys.*, 1963, **34**, 90–97.
- 50 A. Larrañaga and E. Lizundia, *Eur. Polym. J.*, 2019, **121**, 109296.
- 51 Y. Zhu, T. Kwok, J. C. Haug, S. Guo, X. Chen, W. Xu, D. Ravichandran, Y. D. Tchoukalova, J. L. Cornella, J. Yi, O. Shefi, B. L. Vernon, D. G. Lott, J. N. Lancaster and K. Song, *Adv. Mater. Technol.*, 2023, **8**, 2201421.
- 52 M. Elsakhawy and M. Hassan, *Carbohydr. Polym.*, 2007, **67**, 1–10.
- 53 H. Sato, M. Miyada, S. Yamamoto, K. Reddy and Y. Ozaki, *Ether hydrogen bonding along the (110) direction in polyglycolic acid studied by infrared spectroscopy, wide-angle X-ray diffraction, quantum chemical calculations and natural bond orbital calculations*, Royal Society of Chemistry, 2015, vol. 6, pp. 16817–16823.
- 54 L. Lei, Y. Song and R. Chen, *Int. Urogynecol. J.*, 2007, **18**, 603–607.
- 55 C. Tsioptsias, D. Fardis, X. Ntampou, I. Tsivintzelis and C. Panayiotou, *Polymers*, 2023, **15**, 1843.

